Novel Piezoelectric Device for Inducing Strain on Biological Tissue At High Speed

Nicholas Carlisle , *Graduate Student Member, IEEE*, Brian Huynh, Frances M. Wolber, Samuel Rosset , and Ebubekir Avci , *Member, IEEE*

Abstract—A novel mechanically amplified piezoelectric device is presented that induces large complex strains on biological tissue at high speeds. This device allows for the mechanotransduction process (translation of mechanical forces into biochemical signalling) to be studied for different biological tissues, such as single-layered cultured cells on an elastomer membrane or mammalian tissue samples. Two compliant rhombus mechanical amplifiers in a nested configuration are used to overcome the common limitation of piezoelectric actuators of low relative displacement. The device applies a maximum of 84.2% uni-axial tensile strain and a recorded strain rate of 28.8%/ms over a 1 mm long sample, thereby able to reproduce not only physiologically-relevant strain profiles (strains felt by cells from normal bodily function) but also extreme mechanical environments (high strain rates such as from blunt force impacts). A conventional PI feedback controller is implemented to accurately follow complex strain-time profiles with a recorded average standard deviation of 0.12% strain. Experiments such as strain felt by cardiac tissue during a heartbeat or a blunt force impact to the brain causing traumatic brain injury can be realised with the proposed device. Our device will allow researchers to create more accurate simulations of the mechanotransduction processes in vitro, providing the opportunity to gain a greater understanding of different diseases and injuries.

Index Terms—Mechanotransduction, piezoelectric actuator, tissue stretching.

I. INTRODUCTION

LIVING cells of the body can sense and react to the various mechanical environments and strains that are experienced throughout their lifetime. This occurs via a process of translating various mechanical forces into biochemical signalling, which is known as mechanotransduction [1], [2]. It has been documented that mechanical loading plays a fundamental role in the regulation of cell functions, including mutation, migration, differentiation, and cell death [1], [2], [3], [4]. Mutations and abnormal loading conditions can affect this process leading to serious problems and has been linked to many different diseases including muscular dystrophies, osteoarthritis, asthma, cancer, and deafness [1], [3], [5], [6]. Along with studying the link to diseases under physiological conditions, researchers are also investigating the mechanotransduction process during events that go into more extreme mechanical environments leading to cell injuries. Examples include investigating how blunt force affects electrical activation in cardiac tissue [7] and investigating the underlying mechanisms behind blunt force impacts that cause traumatic brain injury (TBI) [8], [9]. Imboden et al. [7] distinguished extreme environments from physiological environments as those where strain is induced at a rate faster than 0.1%–0.2%/ms. Developing methods capable of studying the mechanotransduction process during both physiological and extreme mechanical environments have provided and may continue to provide insight into various diseases and injuries.

Many different methods have been utilized to study the mechanotransduction process. Due to the complexities of conducting studies in vivo, many of these methods focus on using devices to simulate in vivo environments in an in vitro setting. Conducting these experiments external to the body allows for a far less invasive observation, whether via a microscope or other sensors. Likewise, the environment can be held consistent during long experiments. Methods for studying mechanotransduction can be split into three scale approaches where each approach studies a different facet of the process: subcellular scale characterizes physical properties of subcellular components; cellular scale characterizes the mechanical properties of the cell; population-scale studies the biological responses due to mechanical loading [10]. To simulate in vivo environments accurately, studying mechanotransduction at the cellular population scale provides the closest approximation. Two common population scale (cell culture and tissue) in vitro methods are shear flow and substrate stretching [10], [11]. This article focuses on the

latter as it allows for a vast range of experiments such as external forces that cause injury. Substrate stretching works via adhering cultured cells to a deformable structure, typically this is a thin elastomer membrane. Then, the device mechanically actuates this deformable structure, thereby inducing tensile and compressive strains onto the cells [5], [10]. Our proposed stretching device can stretch both elastomer membranes (indirectly stretching cultured cells) and a thin layer of biological tissue (directly stretching cells).

Current state-of-the-art technologies utilize a vast range of actuators to induce strain on the cell samples; common actuators include pneumatic [12], [13], [14], dielectric elastomer actuator (DEA) [7], [15], [16], magnetic [17], [18], [19], [20], and piezoelectric [21], [22], [23], [24]. Along with various methods of actuation, the induced strain can be applied to the cultured cells in a range of forms, including, uniaxial [7], [14], [18], [22], [23], [25], [26], multiaxial [16], radial [27] out-of-plane deformation [13], [15], [21], and even 3-D compression strains [12].

Pneumatic devices provide high strains with relatively low strain rates, meaning they are designed well for producing physiological environments but not extreme mechanical environments. DEA devices are able to produce both extreme and physiological mechanical environments due to their large strains, submillisecond response time, and extremely high strain rates (up to 87%/ms) [16]. However, they require an electric field higher than 100 v/μm to be directly applied to the cell cultures, which may alter the response of electrically sensitive cells such as neurological and cardiac tissue. Moreover, DEA tissue stretching devices are currently limited to feed-forward control in literature [16]. Magnetic actuation devices can simultaneously actuate multiple samples in an array-type layout [18]. These devices often work via adhering cells on top of micropillars. While this allows for a range of different strain patterns, the fabrication and closed-loop control process is more complicated than the aforementioned methods.

Piezoelectric actuation devices provide their inherent abilities of high force density, submillisecond response time, and high displacement resolution into the device [28], [29], [30], [31]. However, their inherent limitation is also present; piezoelectric actuators produce low relative displacements [29], [32], approximately 1 μm displacement per 1 mm in actuator length, severely limiting sample length and maximum strain of these devices. Different methods for negating this problem in literature are as follows: Deguchi et al. [22] coupled a large actuator (84 μm displacement) and small culture samples (100–400 μm) to produce sufficient strain which may limit testing at the population scale. Kamotan et al. [21] developed a Braille display system using piezoelectric pins to produce out-of-plane deformation leaving nonuniform strain patterns across the cell cultures experimental area. Massou et al. [23] proposed a piezoelectric motor, producing gradual strains up to 90% for static stretches. Each approach to overcoming displacement length has been met with its own problems. However, one method is yet to be explored, using a compliant mechanical amplification structure has the potential to produce large strains, over a substantial sample size, without impacting the inherent speed of the actuator. This proposed method has the potential to allow piezoelectric devices to induce both physiological and extreme strain-time profiles.

Presented in this study is a novel design for a piezoelectric tissue stretching device. The proposed design consists of a piezoelectric actuator, coupled with a symmetrical mechanical amplification system and removable culture well. Rhombus mechanical amplifiers have shown great results in amplifying piezoelectric actuators displacement [32], specifically nested rhombus amplifier designs reaching mm range displacement [33], allowing the device to produce greater strains over larger cell population. The removable culture well ensures no contact between active elements (piezoelectric actuator) and cells, reducing possible contamination sources and allowing cells to be cultured while not attached to the device. Based on previously discussed literature surrounding state-of-the-art devices, the minimum requirements for this device to effectively study both physiological and extreme mechanical environments are 25% strain and strain rates (speed) over physiological environments (0.1–0.2%/ms). Requirements for strain rates in extreme mechanical environments are difficult to distinguish for events such as TBI. The higher the strain rate the greater the severity of the injury; therefore, we aim to maximize the strain rate.

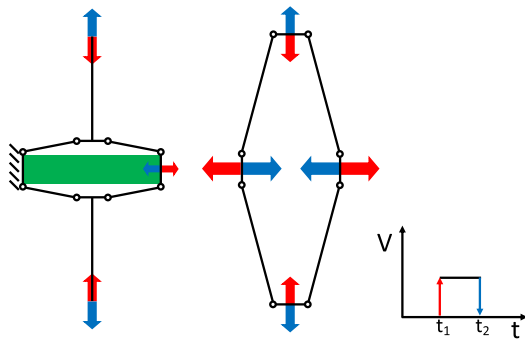The components of this study that contribute to its novelty are as follows.

1) Development of a piezoelectric substrate stretching device that uses a compliant mechanical amplification mechanism to produce a maximum tensile strain of +167.5% and strain rate of 58.6%/ms over a 0.5 mm sample width allowing for the study of both physiological and extreme mechanical environments. To the best of our knowledge, no current piezoelectric substrate stretching device uses mechanical displacement amplification to overcome the small relative displacement length [21], [22], [23].

2) Implement feedback control for precise tracking and recreation of complex strain-time profile to accurately simulate in vivo environments. A proportional-integral (PI) feedback controller is used to achieve this. Current control methods used for tissue stretching devices include feedforward and simple cyclic waveforms limiting the effectiveness of mimicking tissue behavior [15], [16], [18], [34], [35].

The rest of this article is organized as follows. Section II describes the working principles of the device and system configuration. Section III covers the methodology behind the development of all mechanical and control aspects of this device. Section IV discusses the results and effectiveness of the designed system compared to current state-of-the-art devices. Finally, Section V concludes this article.

II. WORKING PRINCIPLES AND SYSTEM CONFIGURATION

A. Working Principles of the Device

The mechanical working principles of the device are shown in Fig. 1. The red arrows show the device during a step-up function, indicating induced tensile strain on the cells. The blue shows the

This article has been accepted for inclusion in a future issue of this journal. Content is final as presented, with the exception of pagination.

CARLISLE et al.: NOVEL PIEZOELECTRIC DEVICE FOR INDUCING STRAIN ON BIOLOGICAL TISSUE AT HIGH SPEED 3

Fig. 1. Mechanical working principles of the device. The structure of the device is shown in black with pivot points indicated by circles. The green rectangle represents the actuator that provides input displacement. Arrows indicate displacement where magnitude is shown by arrow size. Medium arrows are located where amplification structures connect; large arrows are located where the mechanical amplification system connects to the coupling system. The arrows show the phase of the device, red for expansion, and blue for contraction.

device during a step-down function, indicating the device and cells are contracting or returning to their resting state. One side of the inner rhombus is fixed in place and the displacement from the actuator is shown by the small horizontal arrow. The medium vertical arrows indicate the amplified displacement from the inner rhombus and are shown on the second rhombus where the direct connection occurs. The large horizontal arrows show the final output displacement from the outer rhombus amplifier, this displacement causes the strain induced on the cells.

1) *Expansion phase:* A step-up impulse (shown by the red arrows) is applied at $t = t_1$, and the piezoelectric actuator extends producing a very small positive displacement (small horizontal arrow). The inner rhombus then amplifies and inverts this displacement (medium vertical arrows). This displacement couples as the input displacement for the outer rhombus, which is then amplified further and inverted again producing the final output displacement (large horizontal arrow). The arms and coupling mechanism connect to the outer rhombus at the location of these large arrows, allowing this displacement to be directly imparted on the substrate and cells.

2) *Contraction phase:* When the step-down impulse (shown by blue arrows) is applied at $t = t_2$, the piezoelectric actuator contracts causing a contracting input displacement (small horizontal arrow). The inner rhombus amplifies and inverts displacement (medium vertical arrows), which in turn is further amplified and inverted by the outer rhombus producing a contracting output displacement (large horizontal arrows), causing the membrane and cells to contract.

These two phases can be combined in various patterns, speeds, and displacement distances to simulate more complex in vivo strain-time profiles. Furthermore, if the culture well is attached to the device while half or fully actuated, a different resting state voltage can be achieved for the cells, allowing the contraction phase to then be used to produce compressive strains on the cell samples.
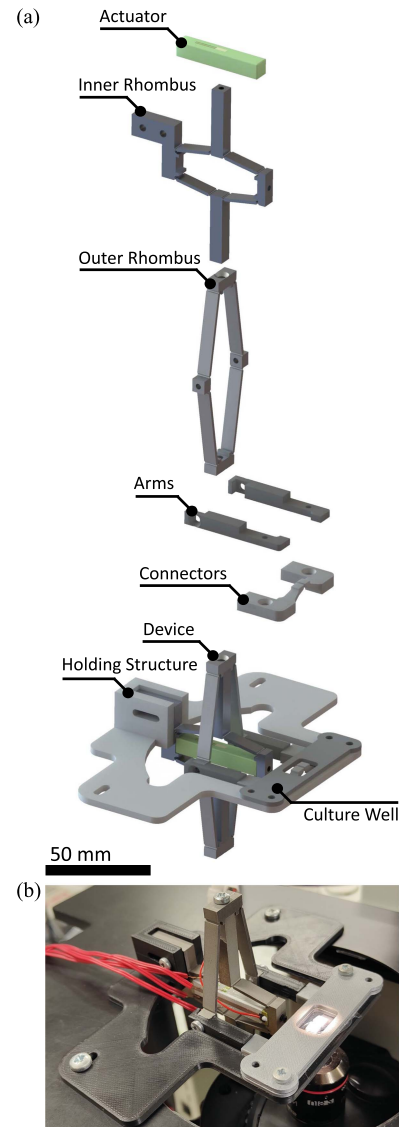
Fig. 2. (a) Mechanical configuration of piezoelectric actuated tissue stretching device. The device consists of a piezoelectric actuator, an inner rhombus mechanical amplifier (first-stage), an outer rhombus mechanical amplifier (second-stage), arms, and connectors (connects the device to cell/tissue samples). In addition, components are culture well (holds the cell samples) and holding structure (holds the system over the microscope and camera). (b) Prototype device over an inverted microscope.

B. System Configuration

Fig. 2(a) shows the configuration of the device in an exploded view of separate components. This device consists of three main systems: 1) the mechanical amplification system, 2) the culture well and coupling system, and 3) the data-gathering system. Fig. 2(b) shows the prototype device over an inverted microscope.

1) Mechanical Amplification System: The actuator used in this device is 40 mm long with a 7 mm × 7 mm cross-section piezoelectric stack actuator (AE0707D44H40DF Tokin, Japan). This actuator accepts voltages between 0 and 150 V to produce a displacement of up to approximately 40 μm. Attached to
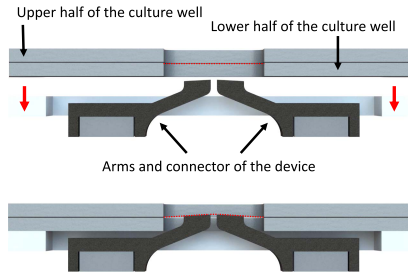
Fig. 3. Design of culture well and coupling method. The red arrows indicate the direction of movement of the culture well during coupling. The red dotted line shows the sample/membrane.

the actuator is a two-part mechanical amplification system. This consists of two rhombus-shaped symmetrical amplification structures in a nested configuration. Simulations of this configuration produce approximately 20x amplification of input displacement (40 μm). The manufacturing method for these rhombus amplifiers is via wire—Electrical Discharge Machining (EDM) and is made from 6 mm thick 6061 T6 Aluminium.

2) Culture Well and Coupling System: The culture well and coupling system consists of a simplistic design, which allows for ease of manufacturing, assembly, and operation. The culture well is made out of two 3-D printed structures that sandwich the stretching substrate. This substrate can be either a thin elastomer membrane that has cells cultured directly on it, or a cell mono-layered tissue such as mammalian mesothelium. The stretching substrate and layers of the culture well are sealed as the culturing process and experiments require the cells to be submerged in solution to ensure the cells are viable. As the entire culture well is designed to be placed in the incubator and has direct contact with the cultured cells, biocompatibility is required. Polylactic acid (PLA) and silicone were chosen as materials, respectively, for the 3-D printed structure and elastomer membrane as they are both considered biocompatible. To connect the cultured sample to the mechanical amplification system, multiple 3-D printed parts are used. The arms of this device are printed with PLA and connected directly to the mechanical amplification system. The connectors are printed with an SLA (stereolithography apparatus) printer and are screwed directly onto the arms, while the other end connects to the bottom of the stretching substrate of the culture well via a double-sided adhesive tape. To ensure that the connection to the stretching substrate is secure, the end of the connectors are designed to have a slight offset and angle that pushes the substrate upward slightly as seen in Fig. 3. This ensures that there is enough force to correctly adhere to the elastomer membrane, likewise adding extra friction ensuring that tissue samples experience adequate strain.

3) Data-Gathering System: The systems control and data gathering setup is shown in Fig. 4. The loop indicated by the red arrows shows the systems control, while the black arrows show the two data-gathering methods. The control loop is set as follows: The system is controlled by a micro-controller (Nucleo-F44RE STMicroelectronics, Switzerland), which reads a desired waveform from a micro SD card. An input signal is then generated and sent to a digital-to-analog converter (DAC) (MX7248JN+ Maxim Integrated, USA) via 12-bit
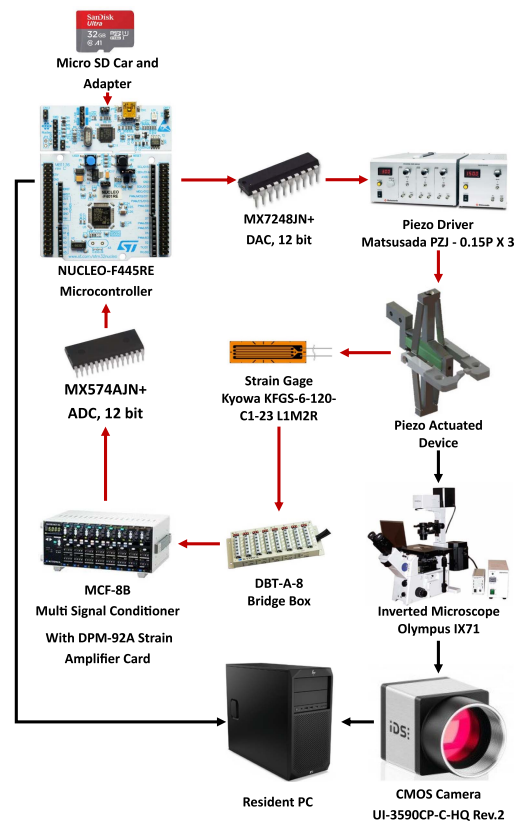

Fig. 4. Control and data-gathering setup for experiments. The red arrows indicate the displacement feedback control loop. The black arrows show the two data-gathering paths for this system, one collects raw data from the controller, and the other collects video of the experiments.

(0-4095 input range) parallel communication, generating a voltage in the 0–10 V range. This voltage is then amplified by the piezoelectric driver (PZJ-0.15PX3 Matsusada, Japan) into a 0–150 V range, which is applied directly to the piezoelectric actuator. The displacement of the piezoelectric actuator is read by four directly adhered strain gages (KFGS-6-120-C1-23 L1M2R Kyowa, Japan) that are connected to the bridge box (DBT-A-8 Kyowa, Japan) in an orthogonal active full-bridge system configuration. This configuration provides a read-out on uniaxial stress while ignoring bending strain and accounting for temperature compensation. The strain gages are rated for self-temperature-compensation between 10 and 100 °C, due to this device requiring to work under biological conditions (36–37 °C) external temperature is controlled, limiting temperature related disturbances. This strain data are then amplified via a strain amplifier card (DPM92-A Kyowa, Japan) in a multisignal conditioner system (MCF-8B Kyowa, Japan). The strain amplifier card is calibrated to give a 0–5 V output for the full range input. The system then reads the amplified strain signal via a 12-bit (0-4096 output over a 0–10 V range) analog-to-digital converter (ADC) (MX574AJN+ Maxim Integrated, USA). The code for this system works as follows: On initialization, the desired waveform consisting of data points every 2 ms is read into an array. During the experiment, an internal interrupt occurs every 2 ms. This interrupt reads the next setpoint into the system from the array, allowing the system to accurately follow the

This article has been accepted for inclusion in a future issue of this journal. Content is final as presented, with the exception of pagination.

CARLISLE et al.: NOVEL PIEZOELECTRIC DEVICE FOR INDUCING STRAIN ON BIOLOGICAL TISSUE AT HIGH SPEED
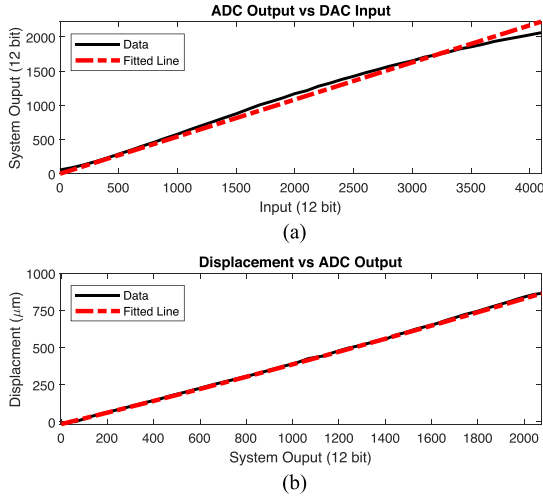
5

Fig. 5. System calibration data. (a) ADC output vs DAC input, fitted with a first-degree polynomial equation. (b) Displacement vs ADC output, fitted with a second-degree polynomial equation.

desired waveform. In addition, during this interrupt, the last set of raw data (containing timestamp, setpoint, and reading) is sent to the PC (black arrow between microcontroller and PC) producing the first path for data-gathering. The main body of the code includes reading the output from the ADC, running the PI controller, and applying the input signal to the DAC; this loops continuously with an approximate duration of 200 μs. The second data-gathering path is for video analysis and real-time viewing of the piezoelectric device. The device and experimental region of interest for the substrate sit directly over an inverted microscope (IX71 Olympus, Japan) giving a clear view of the induced strain or output displacement of the developed system. A COMS camera (UI-3590CP-C-HQ Rev.2 IDS Imaging Development Systems, Germany) links the microscope to the resident PC.

The system is calibrated as follows: System inputs ranging from 0 to 4095 are applied to the DAC in increments of 100, once the actuator has settled to its new length a reading is made from the ADC and an image is captured showing the distance between the arms of the device. The relationship between system input and system output was near linear. Fig. 5(a) shows this data with a fitted trendline giving an equation of $y = 0.5442x$ where "x" is the system input and "y" is the system output. This equation is used to compensate for the difference between input and output in the PI control algorithm. The relationship between ADC output and displacement is also investigated to allow us to generate an accurate waveform. Fig. 5(b) shows this data fitted with a second-degree polynomial giving a trend line of $y = 0.00002x^2 + 0.3861x - 14.317$ where "x" is the system input and "y" is the system output.

III. METHODOLOGY

A. Mechanical Amplification Approach

1) Rhombus Amplifier: The displacement length of the actuator is one of the most common problems faced when working with piezoelectric stack actuators, as these longitudinal actuators
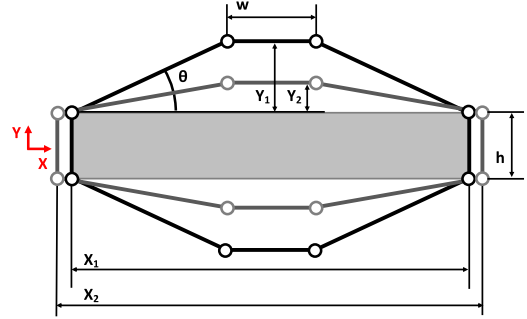

Fig. 6. Amplification principle of a single rhombus amplifier. The *X*-axis follows the input displacement of the device. The *Y*-axis follows the output displacement of the device.

are often only capable of 0.10%–0.15% nominal displacement of the actuator's overall length [36]. As this is a common limitation, different methods have been discussed in the literature to overcome this problem [32], [37].

The advanced mechanical amplification design that showed the most promise for our device is the rhombus design. Fig. 6 shows the amplification principle of a rhombus amplifier in an octagonal shape. Let X_1, h, w, and Y_1 be, respectively, base length of the internal actuator, the height of the internal actuator, the width of the parallel output link, and the distance between the parallel output location and internal actuator at rest. X_2 refers to the actuated length of the internal actuator and is described as

$$X_2 = (1 + \epsilon)X_1 \qquad (1)$$

where ϵ is the strain of the internal actuator. While angle Θ is between $0°$ and $45°$ and the internal actuator extends to length X_2, the distance between the parallel output location (Y_1) decreases by an amplified displacement to be Y_2 where Y_2 is described as

$$Y_2 = \frac{1}{2}\sqrt{4Y_1^2 + 2\epsilon wX_1 - \epsilon(2 + \epsilon)X_1^2}. \qquad (2)$$

From here, amplification (a) can be calculated as

$$a = \frac{2\Delta Y}{\epsilon X_1} \qquad (3)$$

where $\Delta Y = Y_1 - Y_2$. For small values for ϵ amplification factor can be approximated to

$$a = (X_2 - w)/2Y_2 = cot\Theta. \qquad (4)$$

Assuming the flexure joints are perfectly compliant and linkages are perfectly rigid [32], [33]. To maximize amplification, angle Θ needs to be minimized. However, these equations are theoretical and when adding an opposed resistance force to the amplified output, care needs to be taken in choosing Θ to ensure buckling does not occur. This opposing force changes the simple kinematics into a complex mechanics problem [32], therefore, tools like finite element analysis (FEA) in SolidWorks simulation software can assist the design process of such amplifiers.

York et al. [32] presented a rhombus amplification design and explored the design optimisation to achieve an amplification factor of 20x. However, this was under free movement (no output
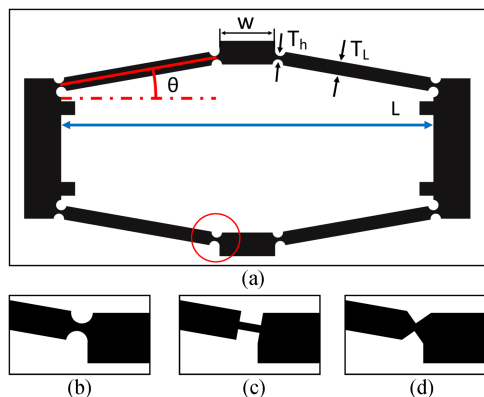
Fig. 7. (a) The rhombus design methodology for mechanical amplification design. (b), (c), and (d) The different pivot geometries simulated.

TABLE I
OPTIMIZED DESIGN VARIABLES FOR MAXIMUM AMPLIFICATION

Variable	Rhombus layer	
	R_1	R_2
L	40 mm	80 mm
w	6 mm	6 mm
T_L	1.5 mm	1.5 mm
Θ	6°	11°
T_h	0.4 mm	0.4 mm
Geometry	Circular (0.55 mm radius)	Circular (0.55 mm radius)

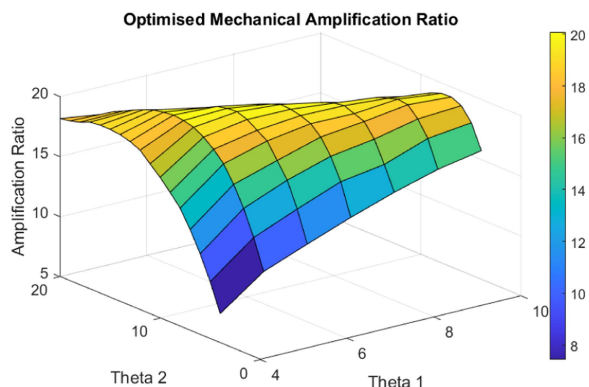
Fig. 8. Results from the optimization process on Θ_1 and Θ_2. Maximum amplification ratio was found at $\Theta_1 = 6°$ and $\Theta_2 = 11°$ with a amplification ratio of 20.1x.

displacement resistance), when taking resistance into account the amplification would decrease. As such, derivative rhombus designs capable of higher amplification were investigated. Ling et al. [38] proposed a design that utilizes a rhombus amplifier, semi-rhombus structure, and level amplifier to create a multistage amplification structure for control of a platform. This design was able to reach mm range displacement, however, the size of the overall structure was large and difficult to fit under a microscope. Ueda et al. [33] proposed a multilayer nested rhombus design that uses an array of six small piezoelectric actuators with rhombus amplifiers, coupled with a larger exterior rhombus amplifier acting as a second layer. With this design, a 2.53 mm displacement was achieved from six 12 mm long piezoelectric actuators. This literature proved that a nested rhombus design would make an attractive design concept for this study. However, for ease of control and overall setup, with a single actuator, a nested mechanical amplification system is designed that has been scarce in near-millimeter range piezoelectric amplification systems. It is noted that a piezoelectric device that uses a rhombus amplifier has been developed for cell stretching at the single cell scale [39]; however, this uses a single rhombus amplifier capable of 11.5x amplification and a manual micromanipulator stage to conduct single cell stretching experiments. While in this study, the aim is to stretch cell cultures/tissue samples in a fully contained device, requiring a larger displacement in a more confined space under a microscope.

2) Mechanical Amplification Design and Optimization: As described in Section II-B1, the proposed device consists of a two-layer nested rhombus mechanical amplification system with a single piezoelectric actuator. The base rhombus design that both layers were developed from is shown in Fig. 7, along with the variables used to optimize each layer's amplification. Variables are shown in Fig. 7(a), where the internal rhombus variables are denoted by $_1$ and outer rhombus variables are denoted by $_2$. Variables L, w, T_L, Θ, and T_h are input displacement resting length, the width of the parallel output link, linkage thickness, angle of linkage relative to input displacement axis, and hinge thickness, respectively. In addition, hinge geometry was also considered as seen in Fig. 7(b)–(d). The process to optimize amplification was completed with the assistance of simulation

using the FEA package in SolidWorks. For accurate simulation, a resistance force is added to account for the elastomer membrane and cultured cells. This force may vary depending on the cells used for specific experiments, therefore, an estimation was made for simulation. The membrane used during experimentation is 50 μm thick Wacker Elastosil film 2030, with a low tensile strength of 6 MPa and maximum elongation of 450%. A 1 mm wide sample stretched to 200% requires a force of 0.4 N. Allowing for additional resistance from cells, a force of 0.5 N was used during the FEA analysis.

The optimized variables are found in Table I where R_x stands for the rhombus amplifier layer. Variable lengths L_1 and L_2 were chosen because of the available space to fit over an inverted microscope. L_1 also indicates the length of the piezoelectric actuator, given a 40 mm long actuator, an assumed input stroke of 40 μm was used during the simulation. The output port length is 6 mm to match the width of the rhombus as stated in Section II-B1 allowing for easy alignment when assembling the two layers of mechanical amplification. Thickness T_L is kept consistent between layers at 1.5 mm to maximize the resistance to linkage bending while minimizing material. Θ_1 and Θ_2 optimum angles were found via a series of FEA simulations varying the angles between $4° < \Theta_1 < 10°$ and $4° < \Theta_2 < 20°$. The simulation results are shown in Fig. 8, where maximum amplification of 20.1x is found at $\Theta_1 = 6°$ and $\Theta_2 = 11°$. Hinge thickness and geometry were found through FEA analysis looking at stress plot and factor of safety (FOS). The circular profile was chosen as the best option as it is easy to consistently and accurately manufacture while minimizing high-stress points. Finally, hinge thickness was found by simulating the FOS plot

TABLE II
PIVOT GEOMETRY THICKNESS RESULTS FROM SIMULATION

Thickness (mm)	Stress (MPa)	FOS	Displacement (μm)
0.2	259.5	1.1	960
0.3	228.1	1.2	830
0.4	193.9	1.4	800
0.5	161.8	1.7	660
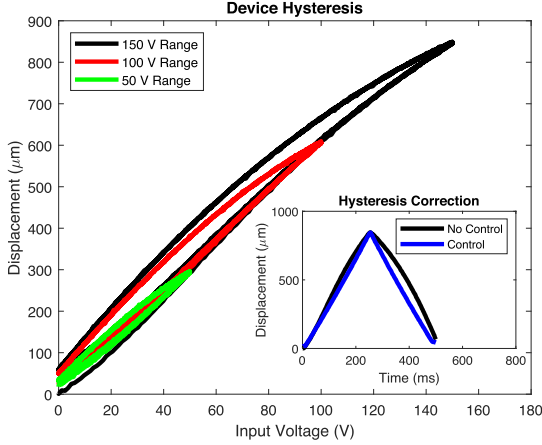
Fig. 9. System hysteresis loops recorded from a 2 Hz triangle wave shown for voltage ranges 0–150, 0–100, and 0–50 Vp-p, respectively with black, red, and yellow lines. Waveform data are recorded over 10 periods. Subfigure shows a 150 Vp-p triangle waveform with (blue line) and without control (black line).

for 0.2 mm $< T_h <$ 0.5 mm where FOS refers to the strength of the system compared to the required load and is calculated as

$$FOS = \frac{\text{Yield Stress}}{\text{Working Stress}} \quad (5)$$

where the yield stress of 6061 T6 Aluminium is 275 MPa. Table II shows results from the simulations; $T_h = 0.4$ mm was chosen as the best option as it had the best mixture of FOS and output displacement.

B. Control Approach

When studying physiological environments in literature, most devices follow simple cyclic waveforms such as sinusoidal [15], [18], [34], [35], or a feedforward approach [16]. To provide a better performance following complex physiological waveforms and overcome the piezoelectric actuators' hysteresis effect, a feedback control algorithm is proposed. Controlling piezoelectric actuators come with their own difficulties as they are well known to exhibit hysteresis loops between input voltage and the associated displacement. Fig. 9 shows hysteresis loops covering three different voltage ranges for the proposed device. For each of the three ranges a 2 Hz triangle waveform is applied and 10 periods of data are recorded. The waveform settles into its hysteresis loop after the first period and has little to no variance in subsequent periods showing the system does not creep over time. The additional subfigure shows the controller's compensation for the hysteresis over the triangle waveform.
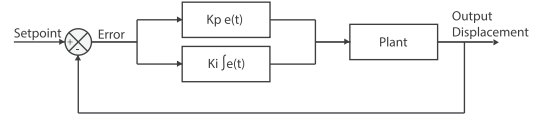
Fig. 10. Conventional PI controller schematic for controlling a piezoelectric actuator's displacement.

As piezoelectric hysteresis effects are well known in literature, many complex models and approaches have been developed over the years. However, when looking at the requirements for the presented device, it was concluded that a conventional PI controller would suffice. PI controllers are an effective method for piezoelectric actuators [30], [40] due to their anti-interference ability and removal of steady-state errors. The implemented PI controller is shown in Fig. 10, and the tuning of this controller was done manually, where $Kp = 1.5$, $Ki = 0.0025$ (waveform period time is calculated in μs), and the error unit is the 12-bit raw output from the ADC. This PI feedback control loop is designed to run at a rate of 5 kHz, where the setpoint is updated at a rate of 50 Hz. The output of this controller is converted to the system input (DAC input) by the equation $y = 1.8375x$ where "x" is the ADC output and "y" is the DAC input, compensating for the linear relationship between input and output.

IV. RESULTS AND DISCUSSION

Experimental results for this device are split into three experiments: 1) characterization, 2) control, and 3) an example tissue stretching application. To provide a realistic experimental environment for the characterization and control experiments, an elastomer membrane was used in place of a tissue or cultured cell sample. For all experiments, an experimental area with a width of 1 mm was used; standard practice in literature uses a minimum width of 0.5 mm [41]; however, a larger experimental area is always encouraged as it allows for larger populations of cells to respond to strain. For the characteristic experiments, a second width of 0.5 mm was also used to show the upper limits of the device under standard practice conditions. Change in width was controlled via printing different-sized connectors (Fig. 2(e)) providing different gaps when assembled.

A. Characterization Results

The characteristic experiment consists of applying a full-range rectangle wave at 2 Hz with a 40% duty cycle controlled via the PI control loop. The frequency of the waveform was chosen as it lined up with the real physiological strain environment used in the control experiment. Fig. 11 shows the displacement response of the device along with the desired waveform (setpoint). The data for this experiment were collected over the first ten periods of the waveform, where the average and standard deviation were calculated for maximum displacement, strain, and strain rate. These values are shown in Table III.

The difference between results from the 1 and 0.5 mm gaps is relatively small, with a drop in displacement of 4.8 μm. This is likely due to the added resistance of stretching the substrate over a 0.5 mm width as opposed to the 1 mm width. Along with
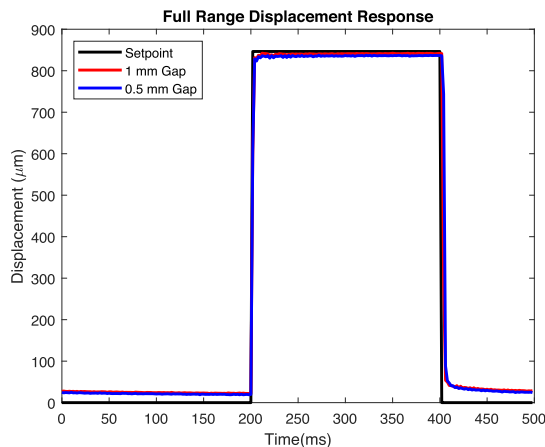
Fig. 11.   Full range displacement response of the system for a 2 Hz rectangle wave with a 40% duty cycle. The desired input waveform is shown in black, the response over a 1 mm wide gap is shown in red and the 0.5 mm gap is shown in blue. Data are averaged over 10 waveforms.

TABLE III
DEVICE CHARACTERISTIC RESULTS OVER 0.5 MM AND 1 MM WIDE SAMPLES AT 2 HZ

Characteristic	0.5 mm sample		1 mm sample	
	Average	Std.dev.	Average	Std.dev.
Displacement (μm)	837.6	1.6	842.4	1.4
Strain (%)	167.5	0.33	84.2	0.14
Strain rate (%/ms)	58.6	3.98	28.8	1.88

this drop in displacement between results, the slight variation between the waveforms increased as evidenced by a rise in standard deviation. However, these variations cause little effect on the overall waveform and performance of the device. Zero displacement for this system was calibrated at complete rest. Due to the nature of piezoelectric actuators, a residual displacement of 20 μm was present during experimentation as can be seen in Fig. 11.

B. Control Results

To test the performance and effectiveness of this device in recreating precise complex strain-time profiles, an in vivo model of the strain experienced in the mitral valve of the human heart was used. This model was supplied by [16]. The waveform consists of a strain range between a 1% compressive strain and a 6% tensile strain throughout 502 ms. Fig. 12(a) shows the result of this experiment conducted under the PI control loop with and without control, where the black line shows the desired waveform (setpoint), the red line shows the system response with control, and the blue line shows the system response without control. The control data were collected and averaged over 60 waveforms with an average standard deviation of 0.12% strain and a maximum deviation of 0.8% (0.008). Allowing the system to run over 60 waveforms (near 30 s) shows that there is no creep over time in the waveform, indicating that the system will stay consistent over long experiments. Fig. 12(b) shows the error throughout the waveform between iterations There is little variation present with the only visible area of interest being a larger consistent negative error coinciding with a spike in strain
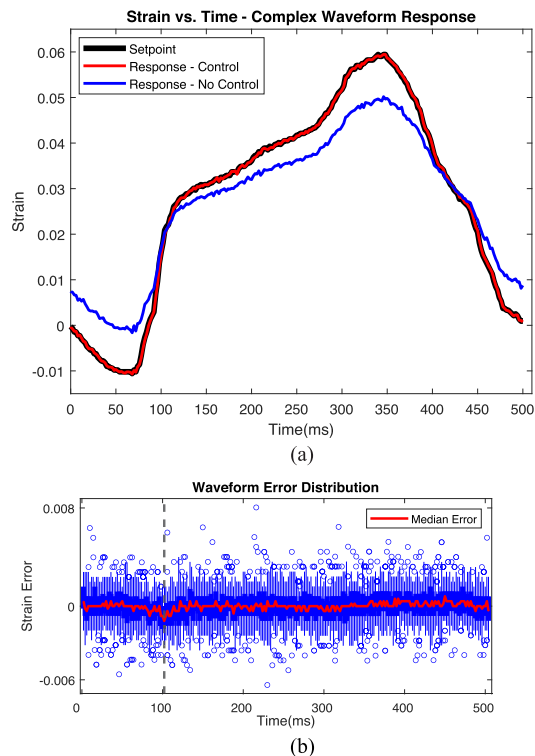

(a)

(b)

Fig. 12.   (a) Strain vs. time graph showing the control response over a complex waveform. The black line shows the in vivo data model taken from the mitral valve of a human heart [16]. The red line shows the system's average response with PI feedback controller over 60 waveforms with a standard deviation of 0.0012 (0.12% strain). The blue line shows the average response without feedback control over 20 waveforms. (b) The error along the control waveform between iterations where the median error is shown in red and the waveform variation location is indicated by the black dashed line (102 ms).

(102 ms). However, this stays within the standard deviation so it is not considered a significant variation. The results from this experiment show that the conventional PI feedback control loop is sufficient for this device to accurately follow complex strain-time profiles to a higher degree than what is previously reported in the literature.

C. Example Application: Stretching Mammalian Tissues

To test how this system performs under real experimental conditions, a test was devised to induce strain on fresh mammalian tissue samples. Guinea pig tissues were retrieved with approval from a euthanized animal after its blood had been collected for another project under AUP 19-76 issued by the Otago University Animal Ethics Committee. A range of tissues were collected and used for experimentation, including, diaphragm, dorsal muscle and fascia, external peritoneum, and stomach tissues. Experimental samples were collected with the aim to be near single-layer tissues for consistency with experiments and imaging. For each tissue sample, two experiments were conducted (Fig. 13): 1) a gradual full-range displacement; 2) the waveform used in control experiments. The standard deviation over the response of the systems between different tissues is calculated for each experiment, a standard deviation of 2.7 μm is

TABLE IV
PERFORMANCE OF STATE-OF-THE-ART DEVICES FOR TENSILE STRAIN AND STRAIN RATE

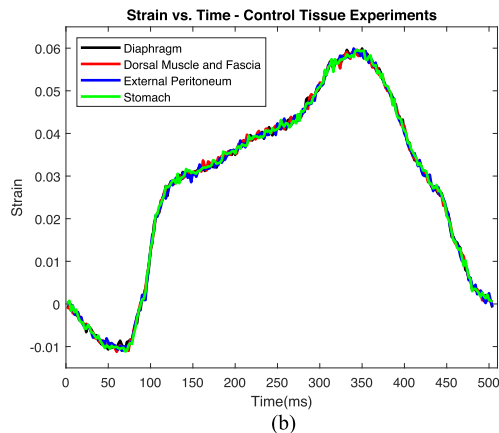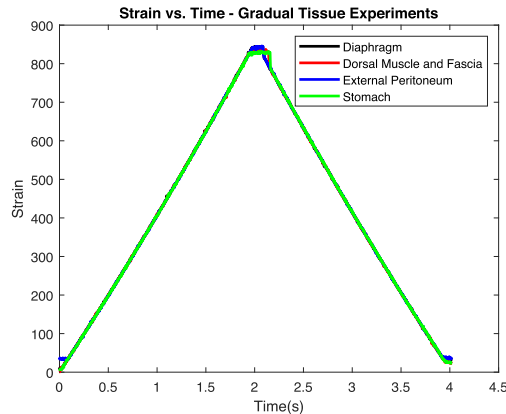| Device type	Max tensile strain (%)	Experimental width (μm)	Strain rate (%/ms)	Control approach	References
Pneumatic	+69	200	6	Cyclic waveform	[14]
DEA	-12 - +38	500	87	Feedforward control	[7], [16]
Magnetic	+25	1800	n/a	Cyclic waveform / static	[20]
Piezoelectric	+30	400	n/a	n/a	[22]
Presented Device	+167.5, +84.2	500, 1000	58.6, 28.8	PI feedback control	

Fig. 13. Experiments on fresh tissues including, diaphragm, dorsal muscle and fascia, external peritoneum, and stomach are represented, respectively, by black, red, blue, and green lines. (a) Gradual tissue experiments over a 4 s period, with a standard deviation of 2.7 μm between tissues. (b) Control tissue experiments with a standard deviation of 0.13% present between tissues.
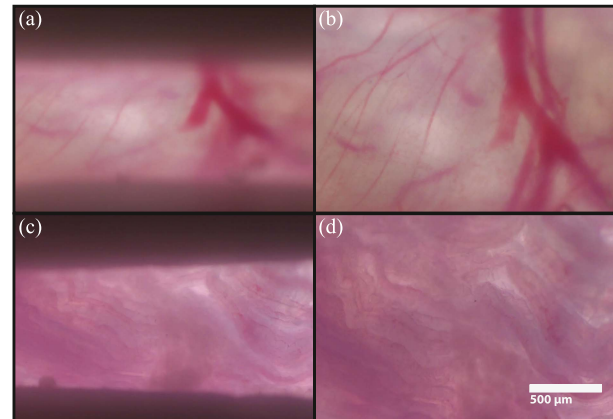

Fig. 14. Images captured during mammalian tissue stretching experiments. (a) and (b) The stomach tissue sample at rest and full displacement. (c) and (d) The external peritoneum tissue sample at rest and full displacement. The dark areas in (a) and (c) are the edge of the connectors and boundary of the experimental region.

present in the gradual tissue experiment, and a standard deviation of 0.13% strain is present in the control tissue experiment. Under real experimental conditions, the control waveform only gained a standard deviation of 0.01% strain when compared to the control experiment results using an elastomer membrane. A small drop in displacement was also present during the gradual time experiment, achieving a maximum displacement of 833.6 μm. This slight decrease in displacement and increase in the control waveforms standard deviation is likely due to the tissue providing slightly more resistance than the elastomer membrane alone.

Fig. 14 shows two examples of the gradual tissue experiment at rest and at full displacement: (a) and (b) show the stomach tissue experiment; c and d show the external peritoneum tissue experiment. This example application proved that the piezoelectric tissue stretching device is capable of stretching tissue layers under real conditions required for biological material. During these experiments, the calculation of strain is reliant solely on the device's readout. Due to the tissues not forming a perfect single layer of cells and some minor out-of-plane movement during actuation, finding reliable points on the tissue sample to measure strain via image analysis is difficult. Therefore, it is expected that there may be a slight discrepancy in the tissues-induced strain. However, as this out-of-plane movement does not visibly change over time, it is reasoned that slippage is not occurring, ensuring any discrepancy is minimal. To ensure this is not a problem in future experiments with cultured cell samples, adding a component of real-time image processing during control, directly measuring cell strain, is suggested.

D. Contribution Summary

Current performance from state-of-the-art devices is shown in Table IV. Strain rates for magnetic and piezoelectric devices were not found to be reported in the literature. The device present in this manuscript can produce +167.5% strain with a strain rate of 58.6%/ms and 84.2% strain with a strain rate of 28.8%/ms, respectively, over a 0.5 and 1 mm experimental width, with only slight decreases in the device's ability present during experimentation under realistic conditions. When comparing performance to the current state-of-the-art devices, the mechanically amplified piezoelectric device far outperforms

other devices in terms of maximum tensile strain, while proving the device's ability to simulate both physiological and extreme mechanical environments. The conventional PI feedback controller provides greater precision when following complex physiological strain-time patterns compared to devices found in literature, inducing more effective mimicked in-vivo environments. Continually improving technology for tissue stretching devices will play an important role in improving the quality of life via unlocking knowledge and therapeutic opportunities associated with diseases and tissue engineering [4].

V. Conclusion

A novel piezoelectric substrate stretching device for inducing strain on single-layered cultured cells and mammalian tissues is presented. The proposed device, consisting of a two-layer nested rhombus mechanical amplification system, is capable of generating up to +167.5% strain with a strain rate of 58.6%/ms and 84.2% strain with a strain rate of 28.8%/ms, respectively, over a 0.5 and 1 mm experimental widths. The conventional PI feedback control loop ensures that this device can create and accurately mimic both physiological and extreme mechanical environments. The simplistic design of this piezoelectric device allows for easy observation over a wide range of possible experiments for minimal expense. The device's capabilities and adaptability show promise in the furtherment of study in the mechanotransduction field by providing the opportunity to study electrically sensitive and other easily contaminated cells such as brain tissue under both physiological and extreme mechanical environments. Future work for this project will include adding a real-time visual component to the feedback control loop, ensuring that cells experience the desired strain, and improving the quality and effectiveness of experiments.
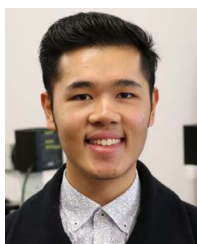
References

[1] D. E. Jaalouk and J. Lammerding, "Mechanotransduction gone awry," *Nature Rev. Mol. Cell Biol.*, vol. 10, no. 1, pp. 63–73, 2009.

[2] M. Maurer and J. Lammerding, "The driving force: Nuclear mechanotransduction in cellular function, fate, and disease," *Annu. Rev. Biomed. Eng.*, vol. 21, pp. 433–468, 2019.

[3] J. H. C. Wang and B. P. Thampatty, "An introductory review of cell mechanobiology," *Biomech. Model. Mechanobiol.*, vol. 5, no. 1, pp. 1–16, 2006.

[4] I. Constantinou and E. E. Bastounis, "Cell-stretching devices: Advances and challenges in biomedical research and live-cell imaging," *Trends Biotechnol.*, vol. 41, no. 7, pp. 939–950, 2023.

[5] A. Poulin, "Miniaturized dielectric elastomer actuator for mechanical stimulation of monolayer cell cultures," *EPFL, Tech. Rep.*, 2016.

[6] S. Giulitti, A. Zambon, F. Michielin, and N. Elvassore, "Mechanotransduction through substrates engineering and microfluidic devices," *Curr. Opin. Chem. Eng.*, vol. 11, pp. 67–76, 2016.

[7] M. Imboden et al., "High-speed mechano-active multielectrode array for investigating rapid stretch effects on cardiac tissue," *Nature Commun.*, vol. 10, no. 1, pp. 1–10, 2019.

[8] Y. H. Wu, S. Rosset, T. R. Lee, M. Dragunow, T. Park, and V. Shim, "In vitro models of traumatic brain injury: A systematic review," *J. Neurotrauma*, vol. 38, no. 17, pp. 2336–2372, 2021.

[9] Y. H. Wu et al., "Analyzing pericytes under mild traumatic brain injury using 3D cultures and dielectric elastomer actuators," *Front. Neurosci.*, vol. 16, 2022, Art. no. 994251.

[10] G. Bao and S. Suresh, "Cell and molecular mechanics of biological materials," *Nature Mater.*, vol. 2, no. 11, pp. 715–725, 2003.

[11] J. Kim, S. Kim, S. Uddin, S. S. Lee, and S. Park, "Microfabricated stretching devices for studying the effects of tensile stress on cells and tissues," *BioChip J.*, vol. 16, no. 4, pp. 366–375, 2022.

[12] C. Moraes, G. Wang, Y. Sun, and C. A. Simmons, "A microfabricated platform for high-throughput unconfined compression of micropatterned biomaterial arrays," *Biomaterials*, vol. 31, no. 3, pp. 577–584, 2010.

[13] H. Kamble, R. Vadivelu, M. Barton, M. J. A. Shiddiky, and N.-T. Nguyen, "Pneumatically actuated cell-stretching array platform for engineering cell patterns in vitro," *Lab a Chip*, vol. 18, no. 5, pp. 765–774, 2018.

[14] Y. Huang and N. T. Nguyen, "A polymeric cell stretching device for real-time imaging with optical microscopy," *Biomed. Microdevices*, vol. 15, no. 6, pp. 1043–1054, 2013.

[15] J. Costa et al., "Bioreactor with electrically deformable curved membranes for mechanical stimulation of cell cultures," *Front. Bioeng. Biotechnol.*, vol. 8, 2020, Art. no. 22.

[16] A. Poulin et al., "An ultra-fast mechanically active cell culture substrate," *Sci. Rep.*, vol. 8, no. 1, pp. 1–10, 2018.

[17] N. J. Sniadecki et al., "Magnetic microposts as an approach to apply forces to living cells," *Proc. Nat. Acad. Sci.*, vol. 104, no. 37, pp. 14553–14558, 2007.

[18] F. Xu et al., "A microfabricated magnetic actuation device for mechanical conditioning of arrays of 3D microtissues," *Lab Chip*, vol. 15, no. 11, pp. 2496–2503, 2015.

[19] C. M. Bidan et al., "Magneto-active substrates for local mechanical stimulation of living cells," *Sci. Rep.*, vol. 8, no. 1, pp. 1–13, 2018.

[20] Á. Enríquez et al., "High-throughput magnetic actuation platform for evaluating the effect of mechanical force on 3D tumor microenvironment," *Adv. Funct. Mater.*, vol. 31, no. 1, 2021, Art. no. 2005021.

[21] Y. Kamotani et al., "Individually programmable cell stretching microwell arrays actuated by a braille display," *Biomaterials*, vol. 29, no. 17, pp. 2646–2655, 2008.

[22] S. Deguchi, S. Kudo, T. S. Matsui, W. Huang, and M. Sato, "Piezoelectric actuator-based cell microstretch device with real-time imaging capability," *AIP Adv.*, vol. 5, no. 6, 2015, Art. no. 067110.

[23] S. Massou et al., "Cell stretching is amplified by active actin remodelling to deform and recruit proteins in mechanosensitive structures," *Nature cell Biol.*, vol. 22, no. 8, pp. 1011–1023, 2020.

[24] D. Mojena-Medina et al., "Design, implementation, and validation of a piezoelectric device to study the effects of dynamic mechanical stimulation on cell proliferation, migration and morphology," *Sensors*, vol. 20, no. 7, pp. 2155–2176, 2020.

[25] N. A. Al Maslamani, A. A. Khilan, and H. F. Horn, "Design of a 3D printed, motorized, uniaxial cell stretcher for microscopic and biochemical analysis of mechanotransduction," *Biol. Open*, vol. 10, no. 2, 2021, Art. no. bio057778.

[26] S. Tsukamoto, T. Asakawa, S. Kimura, N. Takesue, M. R. Mofrad, and N. Sakamoto, "Intranuclear strain in living cells subjected to substrate stretching: A combined experimental and computational study," *J. Biomech.*, vol. 119, 2021, Art. no. 110292.

[27] O. Friedrich, A.-L. Merten, D. Schneidereit, Y. Guo, S. Schürmann, and B. Martinac, "Stretch in focus: 2D inplane cell stretch systems for studies of cardiac mechano-signaling," *Front. Bioeng. Biotechnol.*, vol. 7, 2019, Art. no. 55.

[28] H. Kamble, M. J. Barton, M. Jun, S. Park, and N.-T. Nguyen, "Cell stretching devices as research tools: Engineering and biological considerations," *Lab a Chip*, vol. 16, no. 17, pp. 3193–3203, 2016.

[29] T. Schlinquer, A. Mohand Ousaid, and M. Rakotondrabe, "Displacement amplifier mechanism for piezoelectric actuators design using simp topology optimization approach," in *Proc. IEEE Int. Conf. Robot. Automat.*, 2018, pp. 4305–4311.

[30] E. Avci et al., "High-speed automated manipulation of microobjects using a two-fingered microhand," *IEEE Trans. Ind. Electron.*, vol. 62, no. 2, pp. 1070–1079, Feb. 2015.

This article has been accepted for inclusion in a future issue of this journal. Content is final as presented, with the exception of pagination.

CARLISLE et al.: NOVEL PIEZOELECTRIC DEVICE FOR INDUCING STRAIN ON BIOLOGICAL TISSUE AT HIGH SPEED 11

[31] L. Wang, W. Chen, J. Liu, J. Deng, and Y. Liu, "A review of recent studies on non-resonant piezoelectric actuators," *Mech. Syst. Signal Process.*, vol. 133, 2019, Art. no. 106254.

[32] P. A. York and R. J. Wood, "A geometrically-amplified in-plane piezoelectric actuator for mesoscale robotic systems," in *Proc. IEEE Int. Conf. Robot. Automat.*, 2017, pp. 1263–1268.

[33] J. Ueda, T. W. Secord, and H. H. Asada, "Large effective-strain piezoelectric actuators using nested cellular architecture with exponential strain amplification mechanisms," *IEEE/ASME Trans. Mechatron.*, vol. 15, no. 5, pp. 770–782, Oct. 2010.

[34] J. Kreutzer et al., "Pneumatic unidirectional cell stretching device for mechanobiological studies of cardiomyocytes," *Biomech. Model. Mechanobiol.*, vol. 19, no. 1, pp. 291–303, 2020.

[35] J. Béland, J. E. Duverger, E. Petitjean, A. Maguy, J. Ledoux, and P. Comtois, "Development of an open hardware bioreactor for optimized cardiac cell culture integrating programmable mechanical and electrical stimulations," *AIP Adv.*, vol. 10, no. 3, 2020, Art. no. 035133.

[36] PI Ceramic GmbH, "Displacement modes of piezoelectric actuators." Accessed: Sep. 11, 2021. [Online]. Available: https://www.piceramic.com/en/expertise/piezo-technology/properties-piezo-actuators/displacement-modes/

[37] M. Ling, J. Cao, M. Zeng, J. Lin, and D. J. Inman, "Enhanced mathematical modeling of the displacement amplification ratio for piezoelectric compliant mechanisms," *Smart Mater. Structures*, vol. 25, no. 7, 2016, Art. no. 075022.

[38] M. Ling, J. Cao, Z. Jiang, M. Zeng, and Q. Li, "Optimal design of a piezo-actuated 2-DoF millimeter-range monolithic flexure mechanism with a pseudo-static model," *Mech. Syst. Signal Process.*, vol. 115, pp. 120–131, 2019.

[39] K. Nagayama, S. Yanagihara, and T. Matsumoto, "A novel micro tensile tester with feed-back control for viscoelastic analysis of single isolated smooth muscle cells," *Med. Eng. Phys.*, vol. 29, no. 5, pp. 620–628, 2007.

[40] J. Gan and X. Zhang, "A review of nonlinear hysteresis modeling and control of piezoelectric actuators," *AIP Adv.*, vol. 9, no. 4, 2019.

[41] A. Poulin, C. S. Demir, S. Rosset, T. V. Petrova, and H. Shea, "Dielectric elastomer actuator for mechanical loading of 2D cell cultures," *Lab Chip*, vol. 16, no. 19, pp. 3788–3794, 2016.

Frances M. Wolber received the B.Sc. degree in microbiology and public health from the University of Michigan, Ann Arbor, MI, USA, in 1983, and the Ph.D. degree in pathology from Michigan State University, East Lansing, MI, in 1997.

She is currently a Senior Lecturer and General Manager of the small animal research unit with Massey University, Palmerston North, New Zealand. Her research interests include using cell and animal models to study the effects of food and food components on human health and disease.

Samuel Rosset received the M.Sc. and Ph.D. degrees in microengineering from the EPFL, Lausanne, Switzerland, in 2004 and 2009, respectively.

He is a Senior Research Fellow with the Auckland Bioengineering Institute, University of Auckland, Auckland, New Zealand. Since 2005, he has been working on soft transducers, with a focus on optical and biomedical applications, as well as on the fabrication processes of these devices. His research interests include soft transducers, MEMS, modeling, and fabrication processes.

Nicholas Carlisle (Graduate Student Member, IEEE) received the B.E. (Hons.) degree in mechatronics, in 2021, from Massey University, Palmerston North, New Zealand, where he is currently working toward the Ph.D. degree in microrobotics.

His research interests include microrobotic systems for biomedical applications such as tissue stretching, swarm/collective behavior, and reconfigurable systems at small scales.

Ebubekir Avci (Member, IEEE) received the Ph.D. degree in robotics from Osaka University, Toyonaka, Japan, in 2013.

Between 2014 and 2015, he was a Research Associate with the Hamlyn Centre for Robotic Surgery, Imperial College London, London, U.K.. He is currently a Senior Lecturer in Mechatronics with Massey University, Palmerston North, New Zealand. He is also an Associate Investigator with the MacDiarmid Institute for Advanced Materials and Nanotechnology, Wellington, New Zealand. His research interests include microrobotic systems for biomedical applications such as nanoscale robots for molecule analysis, microscale robots for cell manipulation, and millimeter-scale robots for gut analysis.

Brian Huynh received the B.E. (Hons.) degree in mechatronics from Massey University, Palmerston North, New Zealand, in 2022.

His research interests include robotics in general and piezoelectric actuated mechanisms in particular.